Computational Mechanics (2019) 64:971–988
https://doi.org/10.1007/s00466-019-01690-7

ORIGINAL PAPER

A virtual element method for transversely isotropic elasticity

B. D. Reddy[1] · D. van Huyssteen[2]

Received: 2 October 2018 / Accepted: 20 February 2019 / Published online: 5 March 2019

Abstract
This work studies the approximation of plane problems concerning transversely isotropic elasticity, using a low-order virtual element method (VEM), with a focus on near-incompressibility and near-inextensibility. Additionally, both homogeneous problems, in which the plane of isotropy is fixed; and non-homogeneous problems, in which the fibre direction defining the isotropy plane varies with position, are explored. In the latter case various options are considered for approximating the non-homogeneous fibre directions at an element level. Through a range of numerical examples the VEM approximations are shown to be robust and locking-free for several element geometries and for fibre directions that correspond to both mild and strong non-homogeneity. Further, the convergence rate of the VEM is shown to be comparable to classical low-order standard finite element approaches.

1 Introduction

The popular finite element method has the status of a classical approach for obtaining approximate solutions to problems formulated as systems of partial differential equations or inequalities, or alternatively, in their variational form. Particularly in the domains of solid and fluid mechanics, the method has been used with great success for problems with high degrees of complexity such as non-linear problems and problems with intricate geometries (see for example the treatments in [1,2]).

A number of variants of standard conforming finite element methods have been developed over the last four decades, with a range of motivations in mind. Mixed methods, for example, have allowed all variables of interest to be approximated explicitly; and in addition have provided avenues through which stable and convergent finite element approximations can be developed in situations where the selection of the values of certain parameters might lead to non-convergence. Key examples are those of near-incompressibility, or problems in structural mechanics in which the geometry is characterized by a small length scale. These two features lead, in the context of low-order standard finite element methods, to volumetric and shear locking respectively. Phenomena that are circumvented by the use of mixed methods [3,4].

Yet another variant of the standard conforming finite element method is the discontinuous Galerkin (DG) method, in which interelement continuity is abandoned in favour of greater flexibility with regard to meshing (see for example [5]). In addition, DG methods, when designed appropriately, are stable and uniformly convergent in situations of near-incompressibility for low-order approximations [6–8].

A more recent development in the context of finite element methods is the virtual element method (VEM). In contrast to the geometric restrictions on finite elements, which are most generally triangular or quadrilateral in 2D, and tetrahedral or hexahedral in 3D, the VEM permits elements to be arbitrary polygons in 2D or polyhedra 3D. Furthermore, there is no need for elements to be convex, and degeneracies such as element sides having small interior angles or arbitrarily small edges pose no problems. Some key works in a rapidly growing literature include [9–11]. Applications of the VEM to nonlinear problems include works on nonlinear elasticity [12,13], elastoplasticity [14–16], and contact [17].

Applications of the VEM to elasticity have been largely confined to the isotropic problem, although there have been

✉ D. van Huyssteen
vhydan001@myuct.ac.za

B. D. Reddy
daya.reddy@uct.ac.za

[1] Department of Mathematics and Applied Mathematics and Centre for Research in Computational and Applied Mechanics, University of Cape Town, Rondebosch 7701, South Africa

[2] Department of Mechanical Engineering and Centre for Research in Computational and Applied Mechanics, University of Cape Town, Rondebosch 7701, South Africa

treatments of inextensible materials [18]. Problems involving anisotropic materials pose additional challenges in the context of VEM approaches, particularly for non-homogeneous materials in which the anisotropy varies with position. In [19] limiting extensibility is investigated in an otherwise isotropic material using penalty, Lagrange multiplier, and perturbed Lagrangian approaches. The work was considerably extended in [20]. Here, finite element approximations are studied using both conforming and reduced integration approaches. An error analysis gives an indication of conditions under which low-order approximations are uniformly convergent in the incompressible and inextensible limits, and a set of numerical experiments provides further insight into the conditions under which locking-free behaviour occurs. It is shown that locking-free behaviour occurs in conditions of moderate anisotropy for low-order conforming quadrilaterals, in contrast to the situation for isotropic materials. Furthermore, for high degrees of anisotropy leading to near-inextensibility, locking occurs, but is circumvented by the use of selective under-integration.

Relevant works dealing with the determination or recovery of stress fields for VEM formulations concerning linear elasticity include [21], a stress-displacement mixed VEM, and [22], in which a stress error analysis is presented for an equilibrium-based stress recovery procedure performed on patches of elements. Both works are characterised by adaptation or extension of the standard displacement-based VEM formulation. In [21] the stresses are calculated using constant projection and the displacements are assumed to be constant on an element. The convergence rates of both the stresses and displacements are reported to be approximately equal to 1. In [22], using a patch of elements comprising a central element and those immediately surrounding it a convergence rate of approximately 2 is achieved. However, in the case of a degenerate patch comprising a single element, the convergence rate is reported to be approximately equal to 1.

The purpose of this work is to study low-order VEM approximations for plane problems concerning transversely isotropic elasticity. Of particular interest is the behaviour of VEM approximations for the limiting situations of near-incompressibility and near-inextensibility. Whereas in the case of conventional finite element approximations, as discussed above, some form of modification such as selective under-integration is necessary in order to circumvent locking, VEM approximations exhibit locking-free behaviour in the incompressible and inextensible limits.

A further novel aspect of this work is the treatment of non-homogeneous transverse isotropy; that is, situations in which fibre directions vary with position. Here it becomes necessary to approximate the non-homogeneous terms appropriately in order to preserve the simplicity of the VEM approach, in which integrals are evaluated only on element boundaries. The approximations adopted are shown to be robust, with the locking-free behaviour also evident for the non-homogeneous problem.

The structure of the rest of this work is as follows. Section 2 sets out the details of the constitutive relations for transversely isotropic linear elastic materials, the set of governing equations, and the associated weak formulation. The details of the virtual element method are presented in Sect. 3 and the set of numerical results are presented and discussed in Sect. 4. This work concludes with a summary of results and a discussion of open problems.

2 The governing equations for transverse isotropy

Consider a linear elastic body which occupies a plane, polygonal bounded domain $\Omega \subset \mathbb{R}^2$ with boundary $\partial\Omega$. The boundary comprises a non-trivial Dirichlet part Γ_D and Neumann part Γ_N such that $\Gamma_D \cap \Gamma_N = \emptyset$ and $\overline{\Gamma_D \cup \Gamma_N} = \partial\Omega$.

2.1 The elastic relation

Transversely isotropic materials exhibit isotropic behaviour in a specified plane, this plane being defined by a unit vector $\boldsymbol{a}$ referred to also as the fibre direction.

The Cauchy stress tensor $\boldsymbol{\sigma}$ is related to the infinitesimal strain tensor $\boldsymbol{\varepsilon}$ through the elastic relation

$$\boldsymbol{\sigma} = \mathbb{C}\boldsymbol{\varepsilon}. \tag{2.1}$$

Here $\mathbb{C}$ is a fourth-order tensor of elastic moduli. For a transversely isotropic material (2.1) takes the form [20]

$$\begin{aligned}\boldsymbol{\sigma} = {} & \lambda(\mathrm{tr}\boldsymbol{\varepsilon})\boldsymbol{I} + 2\mu_T\boldsymbol{\varepsilon} + \beta(\boldsymbol{M}:\boldsymbol{\varepsilon})\boldsymbol{M} + \alpha((\boldsymbol{M}:\boldsymbol{\varepsilon})\boldsymbol{I} \\ & + (\mathrm{tr}\boldsymbol{\varepsilon})\boldsymbol{M}) + 2(\mu_L - \mu_T)(\boldsymbol{\varepsilon}\boldsymbol{M} + \boldsymbol{M}\boldsymbol{\varepsilon}).\end{aligned} \tag{2.2}$$

Here $\boldsymbol{M} = \boldsymbol{a} \otimes \boldsymbol{a}$, λ and μ_T are the conventional Lamé parameters, μ_L is the shear modulus in the fibre direction, and $\boldsymbol{I}$ denotes the second-order identity tensor. The material constants α and β do not have a direct interpretation, though it will be seen that $\beta \to \infty$ in the limit of inextensible behaviour in the fibre direction.

The special case of an isotropic material is recovered by setting $\alpha = \beta = 0$ and $\mu_L = \mu_T$.

The five material constants in (2.2) may be related to the "engineering" constants, viz. Young's moduli E_L and E_T in the fibre direction and plane of isotropy, respectively, and the corresponding Poisson's ratios ν_L and ν_T, by inverting (2.2), specializing it to the case in which $\boldsymbol{a} = \boldsymbol{e}_3$, and comparing it with the compliance relation written in the form (see for example [23])

$$\begin{pmatrix} \varepsilon_{11} \\ \varepsilon_{22} \\ \varepsilon_{33} \\ 2\varepsilon_{23} \\ 2\varepsilon_{13} \\ 2\varepsilon_{12} \end{pmatrix} = \begin{pmatrix} \frac{1}{E_T} & -\frac{\nu_T}{E_T} & -\frac{\nu_L}{E_L} & 0 & 0 & 0 \\ -\frac{\nu_T}{E_T} & \frac{1}{E_T} & -\frac{\nu_L}{E_L} & 0 & 0 & 0 \\ -\frac{\nu_L}{E_L} & -\frac{\nu_L}{E_L} & \frac{1}{E_L} & 0 & 0 & 0 \\ 0 & 0 & 0 & \frac{1}{\mu_L} & 0 & 0 \\ 0 & 0 & 0 & 0 & \frac{1}{\mu_L} & 0 \\ 0 & 0 & 0 & 0 & 0 & \frac{1}{\mu_T} \end{pmatrix} \begin{pmatrix} \sigma_{11} \\ \sigma_{22} \\ \sigma_{33} \\ \sigma_{23} \\ \sigma_{13} \\ \sigma_{12} \end{pmatrix}. \tag{2.3}$$

For the purposes of a parametric study we make the assumption for the remainder of this work that

$$\nu_T = \nu_L := \nu \quad \text{and} \quad \mu_T = \mu_L := \mu. \tag{2.4}$$

Further, we set

$$p = \frac{E_L}{E_T}, \tag{2.5}$$

so that the parameter p measures the degree of transverse isotropy, with inextensible behaviour corresponding to the limit $p \to \infty$. Note that this is not equivalent to the case of limiting extensibility in an otherwise isotropic material as presented in [19], which would require, in addition, that $\alpha = 0$.

The parameters in (2.2) may then be expressed in terms of the engineering parameters as [20]

$$\begin{aligned} \frac{\lambda}{E_T} &= \frac{\nu(\nu + p)}{D}, \\ \frac{\alpha}{E_T} &= \frac{\nu^2(p-1)}{D}, \\ \frac{\beta}{E_T} &= \frac{p^2(1-\nu^2) - p(1+2\nu^2) + 3\nu^2}{D}, \end{aligned} \tag{2.6}$$

in which the denominator D is given by

$$D = (1+\nu)(p(1-\nu) - 2\nu^2)\,. \tag{2.7}$$

We also have the relation

$$\mu_T = \frac{E_T}{2(1+\nu)}\,. \tag{2.8}$$

We now consider the case of incompressible behaviour in which $\mathrm{tr}\boldsymbol{\varepsilon} = 0$. With the assumptions (2.4) and the relation (2.5) we have from (2.3)

$$\mathrm{tr}\boldsymbol{\varepsilon} = \frac{1}{E_T}\left(1 - \nu - \frac{\nu}{p}\right)\sigma_{11} + \frac{1}{E_T}\left(1 - \nu - \frac{\nu}{p}\right)\sigma_{22} + \frac{1}{pE_T}(1-2\nu)\sigma_{33}. \tag{2.9}$$

For the most general case of $\sigma_{11}, \sigma_{22}, \sigma_{33} \neq 0$, $\mathrm{tr}\boldsymbol{\varepsilon} = 0$ if and only if

$$\begin{cases} \nu = \frac{p}{p+1} \\ \nu = \frac{1}{2} \end{cases} \quad \Leftrightarrow \quad p = 1 \quad \text{and} \quad \nu = \frac{1}{2}. \tag{2.10}$$

Thus incompressible behaviour is only possible in the isotropic case. In the case of plane strain with $\varepsilon_{22} = 0$ and eliminating σ_{22}, we have

$$\mathrm{tr}\boldsymbol{\varepsilon} = \frac{1}{E_T}\left(1 - \nu^2 - \frac{\nu^2}{p} - \frac{\nu}{p}\right)\sigma_{11} + \frac{1}{pE_T}\left(1 - \nu - \nu^2 - \frac{\nu^2}{p}\right)\sigma_{33}. \tag{2.11}$$

Assuming $\sigma_{11}, \sigma_{33} \neq 0$, $\mathrm{tr}\boldsymbol{\varepsilon} = 0$ if and only if

$$\begin{cases} \nu = \frac{p}{p+1} \\ \nu = \frac{1}{2} \end{cases} \quad \Leftrightarrow \quad p = 1 \quad \text{and} \quad \nu = \frac{1}{2}. \tag{2.12}$$

We thus have the same conditions for incompressibility as in the general 3D case (2.10).

Furthermore, noting that $D \to 0$ in the incompressible limit, $\nu \to \frac{1}{2}$ when $p \to 1$, it is evident from (2.6) and (2.7) that

$$\begin{cases} \lambda \text{ is bounded as } \nu \to \frac{1}{2}, \text{ if } p > 1, \\ \text{ and as } p \to \infty \text{ (inextensibility)} \\ \lambda \to \infty \text{ as } \nu \to \frac{1}{2}, \text{ for } p = 1 \text{ (isotropy)} \end{cases} \tag{2.13}$$

$$\begin{cases} \alpha \text{ is bounded as } \nu \to \frac{1}{2}, \text{ if } p > 1 \\ \alpha \to 0 \text{ as } p \to 1 \text{ (isotropy)} \end{cases} \tag{2.14}$$

$$\begin{cases} \beta \text{ is bounded as } \nu \to \frac{1}{2}, \text{ if } p > 1 \\ \beta \to \infty \text{ as } p \to \infty \text{ (inextensibility)}\,. \end{cases} \tag{2.15}$$

The elasticity tensor is assumed to be pointwise stable; that is, to satisfy the condition

$$\boldsymbol{\varepsilon} : \mathbb{C}\boldsymbol{\varepsilon} > 0 \quad \text{for all } \boldsymbol{\varepsilon}\,.$$

General conditions on the material constants for pointwise stability are readily available, see for example [24], and are given by

$$E_L > 0 \quad E_T > 0 \quad \nu_L > 0 \quad \nu_T > 0, \tag{2.16a}$$

$$-1 < \nu_T^2 < 1, \tag{2.16b}$$

$$\nu_L^2 < p, \tag{2.16c}$$

$$1 - 2\nu_L^2 p > \nu_T. \tag{2.16d}$$

We henceforth assume (2.16) to hold.

2.2 Governing equations

The body is subjected to a body force $\boldsymbol{f}$, prescribed loading $\boldsymbol{h}$ on Γ_N, and a prescribed displacement $\boldsymbol{g}$ on Γ_D.

The equation of equilibrium is

$$-\operatorname{div}\boldsymbol{\sigma} = \boldsymbol{f} \qquad \text{on } \Omega. \tag{2.17}$$

Small displacements are assumed, and the strain displacement relation is given by

$$\boldsymbol{\varepsilon}(\boldsymbol{u}) = \frac{1}{2}(\nabla\boldsymbol{u} + [\nabla\boldsymbol{u}]^T) \qquad \text{or} \qquad \varepsilon_{ij}(\boldsymbol{u}) = \frac{1}{2}(u_{i,j} + u_{j,i}). \tag{2.18}$$

Here $\boldsymbol{u}$ denotes the displacement, and $\nabla\boldsymbol{u}$ the displacement gradient with components $u_{i,j}$. Here and henceforth we choose a fixed Cartesian coordinate system x_i with orthonormal basis $\boldsymbol{e}_i$.

The boundary conditions are

$$\boldsymbol{u} = \boldsymbol{g} \qquad \text{on } \Gamma_D, \tag{2.19a}$$

$$\boldsymbol{\sigma}\cdot\boldsymbol{n} = \boldsymbol{h} \qquad \text{on } \Gamma_N. \tag{2.19b}$$

Equations (2.17)–(2.19), together with the elastic relation (2.2), constitute the boundary-value problem for a transversely isotropic body.

2.3 Weak formulation

We denote by $L^2(\Omega)$ the space of square-integrable functions on Ω, and by $H^1(\Omega)$ the Sobolev space of functions which, together with their generalized first derivatives, are square-integrable, and set $V = [H^1_D(\Omega)]^d = \{\boldsymbol{v} \mid v_i \in H^1(\Omega),\ \boldsymbol{v} = \boldsymbol{0} \text{ on } \Gamma_D\}$.

We also define the function $\boldsymbol{u}_g \in [H^1(\Omega)]^d$ such that

$$\boldsymbol{u}_g\big|_{\Gamma_D} = \boldsymbol{g}\,.$$

The bilinear form $a(\cdot,\cdot)$ and linear functional $\ell(\cdot)$ are defined by

$$a : [H^1(\Omega)]^d \times [H^1(\Omega)]^d \to \mathbb{R},$$

$$a(\boldsymbol{u},\boldsymbol{v}) = \int_\Omega \boldsymbol{\sigma}(\boldsymbol{u}) : \boldsymbol{\varepsilon}(\boldsymbol{v})\, dx, \tag{2.20a}$$

$$l : [H^1(\Omega)]^d \to \mathbb{R},$$

$$\ell(\boldsymbol{v}) = \int_\Omega \boldsymbol{f}\cdot\boldsymbol{v}\, dx + \int_{\Gamma_N} \boldsymbol{h}\cdot\boldsymbol{v}\, ds - a(\boldsymbol{u}_g,\boldsymbol{v}). \tag{2.20b}$$

The weak form of the problem is then as follows: given $\boldsymbol{f} \in [L^2(\Omega)]^d$ and $\boldsymbol{h} \in [L^2(\Gamma_N)]^d$, find $\boldsymbol{U} \in [H^1(\Omega)]^d$ such that

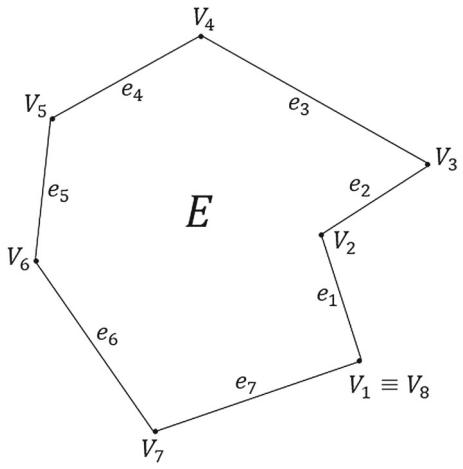

Fig. 1 An arbitrary virtual element

$\boldsymbol{U} = \boldsymbol{u} + \boldsymbol{u}_g$, $\boldsymbol{u} \in V$, and

$$a(\boldsymbol{u},\boldsymbol{v}) = \ell(\boldsymbol{v}) \qquad \forall \boldsymbol{v} \in V. \tag{2.21}$$

We write the bilinear form as

$$a(\boldsymbol{u},\boldsymbol{v}) = a^{\text{iso}}(\boldsymbol{u},\boldsymbol{v}) + a^{\text{ti}}(\boldsymbol{u},\boldsymbol{v}), \tag{2.22}$$

where

$$a^{\text{iso}}(\boldsymbol{u},\boldsymbol{v}) = \lambda\int_\Omega (\nabla\cdot\boldsymbol{u})(\nabla\cdot\boldsymbol{v})\, dx + 2\mu\int_\Omega \boldsymbol{\varepsilon}(\boldsymbol{u}) : \boldsymbol{\varepsilon}(\boldsymbol{v})\, dx, \tag{2.23a}$$

$$\begin{aligned} a^{\text{ti}}(\boldsymbol{u},\boldsymbol{v}) = \alpha\int_\Omega &[(\boldsymbol{M} : \boldsymbol{\varepsilon}(\boldsymbol{u}))(\nabla\cdot\boldsymbol{v}) \\ &+ (\nabla\cdot\boldsymbol{u})(\boldsymbol{M} : \boldsymbol{\varepsilon}(\boldsymbol{v}))]\, dx \\ &+ \beta\int_\Omega (\boldsymbol{M} : \boldsymbol{\varepsilon}(\boldsymbol{u}))(\boldsymbol{M} : \boldsymbol{\varepsilon}(\boldsymbol{v}))\, dx\,. \end{aligned} \tag{2.23b}$$

The bilinear form is clearly symmetric. The well-posedness of the weak problem requires the bilinear form to be continuous and coercive, and the linear functional continuous. With the assumptions in (2.16), it is shown in [20] that the problem has a unique solution that depends continuously on the data.

3 The virtual element method

The domain Ω is partitioned into a mesh of elements comprising non-overlapping polygons E with $\overline{\cup E} = \bar{\Omega}$. A typical polygonal element is shown in Fig. 1. We denote by e_i the edge connecting vertices V_i and V_{i+1} with $i = 1,\ldots,N$, where N is the total number of vertices of element E.

We construct a conforming approximation in a space $V^h \subset V$. The space V^h comprises functions that are con-

tinuous on Ω, piecewise linear on the boundary ∂E of each element, and with $\operatorname{div} \mathbb{C}\boldsymbol{\varepsilon}(\boldsymbol{v}_h)$ vanishing on E [9,10]:

$$V^h = \{\boldsymbol{v}_h \in V \mid \boldsymbol{v}_h \in [C(\Omega)]^2, \quad (3.1)$$
$$\operatorname{div} \mathbb{C}\boldsymbol{\varepsilon}(\boldsymbol{v}_h) = \boldsymbol{0} \text{ on } E,\ \boldsymbol{v}_h|_e \in P_1(e)\}\,.$$

Here and henceforth $P_k(X)$ denotes the space of polynomials of degree $\leq k$ on the set $X \subset \mathbb{R}^d$ $(d = 1, 2)$. We assign degrees of freedom to the nodes, which are located at the element vertices, and write, for each element,

$$\boldsymbol{v}_h|_E = \boldsymbol{\varphi}\boldsymbol{d} \quad (3.2)$$

in which $\boldsymbol{\varphi}$ denotes a matrix of virtual basis functions, and $\boldsymbol{d}$ is the $2N \times 1$ vector of degrees of freedom.

All computations are carried out on the edges e of elements, and it is convenient to write also

$$\boldsymbol{v}_h|_{\partial E} = \boldsymbol{N}\boldsymbol{d} \quad \text{and} \quad \boldsymbol{\varepsilon}(\boldsymbol{v}_h) = \boldsymbol{B}\boldsymbol{d}\,, \quad (3.3)$$

in which $\boldsymbol{N}$ and $\boldsymbol{B}$ are respectively matrices of standard Lagrangian linear basis functions and their derivatives. Thus, the basis functions $\boldsymbol{\varphi}$ are not known, and are not required to be known; their traces on the boundary are however required, and are simple Lagrangian functions.

We will require the projection $\Pi : V_h|_E \to P_0(E)$, defined on E by

$$\int_E \Pi\boldsymbol{v}_h \, dx = \int_E \boldsymbol{\varepsilon}(\boldsymbol{v}_h) \, dx\,. \quad (3.4)$$

Thus Π is the L^2-orthogonal projection onto constants of the strain associated with the displacement $\boldsymbol{v}_h$ on an element E. From (3.3), and given that $\Pi\boldsymbol{v}_h$ is constant we have, in component form,

$$\begin{aligned}(\Pi\boldsymbol{v}_h)_{ij} &= \frac{1}{2}\frac{1}{|E|}\int_E ((v_h)_{i,j} + (v_h)_{j,i})\, dx \\ &= \frac{1}{2}\frac{1}{|E|}\oint_{\partial E} ((v_h)_i n_j + (v_h)_j n_i)\, ds \\ &= \frac{1}{2}\frac{1}{|E|}\sum_{e\in\partial E}\int_e (N_{iA} d_A^E n_j + N_{jA} d_A^E n_i)\, ds\,. \end{aligned} \quad (3.5)$$

Here d_A^E denotes the degrees of freedom associated with element E, summation is implied over all repeated indices, and we have used integration by parts and the representation $(3.3)_1$. The integrals in (3.5) are readily evaluated as the edge basis functions are known. Thus the projection $\Pi\boldsymbol{v}_h$ is available as a function of the degrees of freedom.

To construct the virtual element formulation we start by writing

$$a^E(\boldsymbol{u}, \boldsymbol{v}) := a(\boldsymbol{v}, \boldsymbol{v})|_E$$
$$= \int_E \boldsymbol{\varepsilon}(\boldsymbol{u}_h) : \mathbb{C}\boldsymbol{\varepsilon}(\boldsymbol{v}_h)\, dx\,, \quad (3.6)$$

so that $a^E(\cdot,\cdot)$ denotes the contribution of element E to the bilinear form $a(\cdot,\cdot)$ defined in (2.20a). Considering (3.4) we have

$$\begin{aligned} a^E(\boldsymbol{u}_h, \boldsymbol{v}_h) &= \int_E \Pi\boldsymbol{u}_h : \mathbb{C}\Pi\boldsymbol{v}_h \, dx \\ &\quad + \int_E (\boldsymbol{\varepsilon}(\boldsymbol{u}_h) - \Pi\boldsymbol{u}_h) : \mathbb{C}(\boldsymbol{\varepsilon}(\boldsymbol{v}_h) - \Pi\boldsymbol{v}_h)\, dx \quad (3.7a) \\ &\quad + \int_E \Pi\boldsymbol{u}_h : \mathbb{C}(\boldsymbol{\varepsilon}(\boldsymbol{v}_h) - \Pi\boldsymbol{v}_h)\, dx \\ &\quad + \int_E (\boldsymbol{\varepsilon}(\boldsymbol{u}_h) - \Pi\boldsymbol{u}_h) : \mathbb{C}\Pi\boldsymbol{v}_h \, dx \quad (3.7b) \\ &= \int_E \Pi\boldsymbol{u}_h : \mathbb{C}\Pi\boldsymbol{v}_h \, dx + \int_E (\boldsymbol{\varepsilon}(\boldsymbol{u}_h) \\ &\quad - \Pi\boldsymbol{u}_h) : \mathbb{C}(\boldsymbol{\varepsilon}(\boldsymbol{v}_h) - \Pi\boldsymbol{v}_h)\, dx \quad (3.7c) \\ &= \underbrace{\int_E \Pi\boldsymbol{u}_h : \mathbb{C}\Pi\boldsymbol{v}_h \, dx}_{\text{consistency term}} \\ &\quad + \underbrace{\int_E \left[\boldsymbol{\varepsilon}(\boldsymbol{u}_h) : \mathbb{C}\boldsymbol{\varepsilon}(\boldsymbol{v}_h) - \Pi\boldsymbol{u}_h : \mathbb{C}\Pi\boldsymbol{v}_h\right] dx}_{\text{stabilisation term}}\,. \quad (3.7d) \end{aligned}$$

The last line is obtained by noting the definition of the projection operator, so that the two terms in (3.7b) are zero. Furthermore, the definition of the projection is invoked again in going from (3.7c) to (3.7d). The terms in (3.7d) are referred to respectively as the consistency term and stabilisation term.

The consistency term After substitution of (3.5) in the consistency term, evaluation of the integral leads to the expression

$$\int_E \Pi\boldsymbol{u}_h : \mathbb{C}\Pi\boldsymbol{v}_h \, dx = (\bar{\boldsymbol{d}})^T \boldsymbol{K}^E_{\text{con}}\boldsymbol{d} \quad (3.8)$$

in which $\boldsymbol{K}^E_{\text{con}}$ is the consistency stiffness matrix for element E and $\boldsymbol{d}^E$ and $\bar{\boldsymbol{d}}^E$ are respectively the vectors of nodal degrees of freedom of $\boldsymbol{u}_h$ and $\boldsymbol{v}_h$ on element E.

The stabilisation term Use of the consistency term alone would lead to a rank-deficient stiffness matrix. The second term on the right hand side of (3.7d) serves the purpose of stabilising the formulation. The basic idea behind the VEM is that integrals are evaluated on the boundaries of elements only; the stabilisation term in its original form would require that integrals be evaluated on the elements. Nevertheless, it is not necessary to evaluate this term exactly, and it suffices to

replace it with an approximation. There are several methods that can be employed, see for example [11,15]. However, we choose the robust stabilisation method presented in [25], and defined by

$$a^E_{\text{stab}}(\boldsymbol{u}_h, \boldsymbol{v}_h) = \tau \overline{\boldsymbol{d}}^T [\boldsymbol{I} - \boldsymbol{D}(\boldsymbol{D}^T\boldsymbol{D})^{-1}\boldsymbol{D}^T]\boldsymbol{d}\,. \tag{3.9}$$

Here $\overline{\boldsymbol{d}}$ and $\boldsymbol{d}$ are, again, respectively the vectors of nodal degrees of freedom associated with $\boldsymbol{v}_h$ and $\boldsymbol{u}_h$, and $\boldsymbol{D}$ is the matrix that relates the nodal degrees of freedom $\boldsymbol{d}_1$ of a linear vector polynomial to its degrees of freedom $\boldsymbol{s}$ relative to a scaled linear monomial basis. That is, for an element with N nodes,

$$\boldsymbol{d}_1 = \boldsymbol{D}\boldsymbol{s}\,. \tag{3.10}$$

Note that $\boldsymbol{D}$ has dimensions $2N \times 6$, and has the basis monomials

$$\boldsymbol{\mathcal{M}} = \{1, \xi, \eta\} = \left\{1, \frac{x - x_c}{d_E}, \frac{y - y_c}{d_E}\right\}, \tag{3.11}$$

where d_E is the diameter of element E, with x_c and y_c the $x-$ and $y-$coordinates of the centroid of E respectively. This approximation may be motivated by seeking a stabilisation term of the form

$$\tau(\boldsymbol{d}^T\boldsymbol{d} - \boldsymbol{d}_1^T\boldsymbol{d}_1) \tag{3.12}$$

in which $\boldsymbol{d}_1$ are the nodal degrees of freedom of a linear polynomial that is closest to $\boldsymbol{u}_h$ in some sense, and τ is a suitable scalar to be chosen. In the event that $\boldsymbol{u}_h$ is a linear polynomial this term vanishes of course.

From (3.10) we have

$$\begin{aligned}\boldsymbol{d}_1^T\boldsymbol{d}_1 &= (\boldsymbol{s}^T\boldsymbol{D}^T)(\boldsymbol{D}\boldsymbol{s})\\ &= \boldsymbol{s}^T(\boldsymbol{D}^T\boldsymbol{D})(\boldsymbol{D}^T\boldsymbol{D})^{-1}(\boldsymbol{D}^T\boldsymbol{D})\boldsymbol{s}\\ &= \boldsymbol{d}_1^T\boldsymbol{D}(\boldsymbol{D}^T\boldsymbol{D})^{-1}\boldsymbol{D}^T\boldsymbol{d}_1\,.\end{aligned} \tag{3.13}$$

Then we obtain (3.9) by replacing $\boldsymbol{d}_1$ with the actual vector degrees of freedom.

We need to choose a suitable value for the scalar τ, such that it is some value representative of the constitutive tensor. We consider the transversely isotropic material properties λ, α, β, μ_L and μ_T. As seen in Sect. 2.1 $\lambda, \beta \to \infty$ as $\nu \to 0.5$, to keep the VEM locking-free we therefore reject these options. We choose $\tau = \mu_T$ as it is bounded and is representative of both isotropic and transversely isotropic materials. As we have set $\mu := \mu_L = \mu_T$, we then have

$$\boldsymbol{K}^E_{\text{stab}} = \mu\left[\boldsymbol{I} - \boldsymbol{D}\left(\boldsymbol{D}^T\boldsymbol{D}\right)^{-1}\boldsymbol{D}^T\right]. \tag{3.14}$$

As we have used scaled coordinates, no area scaling of the stabilisation term is necessary. The complete stiffness matrix is then given by

$$\boldsymbol{K}^E = \boldsymbol{K}^E_{\text{con}} + \boldsymbol{K}^E_{\text{stab}}. \tag{3.15}$$

4 Numerical results

In this section we present numerical results for three model problems to illustrate the performance of the VEM. We consider homogeneous materials, for which the plane of isotropy is fixed across the domain, and also non-homogenous materials, for which the plane of isotropy, as defined by the vector $\boldsymbol{a}$, varies with position. Plane strain conditions are assumed. As in Sect. 2.1 we set $\nu_T = \nu_L = \nu$ and $\mu_T = \mu_L = \mu$. We consider values of $p \geq 1$, unless stated otherwise, and Poisson's ratio of $\nu = 0.3$ or, to test behaviour in the near-incompressible limit, $\nu = 0.49995$. In all cases the conditions for pointwise stability (2.16) are met.

We define $\hat{a} := \widehat{(Ox, \boldsymbol{a})}$ to be the angle between the x-axis and the fibre direction $\boldsymbol{a}$. The results in the examples that follow are obtained for the following element types:

Q_1	The standard bilinear quadrilateral
Q_2	The standard biquadratic quadrilateral
Quad	The VEM formulation with four-noded elements
Hex	The VEM formulation with six-noded elements
Voronoi	The VEM formulation with Voronoi elements

Figure 2 depicts patches of the meshes comprising six-noded and Voronoi elements for a mesh density d of 7, where $d = \sqrt{n_{elements}}$. Meshes are constructed on a reference domain and then mapped to the problem domain, Fig. 2 depicts meshes after this mapping.

4.1 Constant fibre direction

We present results here for the case in which fibre directions are constant on the domain. The emphasis is on near-incompressibility and near-inextensibility, either separately or combined. Unless indicated otherwise, in the examples that follow Poisson's ratio is set at $\nu = 0.49995$. To satisfy the conditions for pointwise stability (2.16) we require, for $\nu = 0.49995$, that $p > 0.9997$. Thus, for simplicity, we consider the range $p \geq 1$ in which $p = 1$ corresponds to the near-incompressible limit.

Cook's membrane problem This problem consists of a trapezoidal panel fully fixed along its left edge with a uniformly distributed load along its right edge, as shown in Fig. 3. The applied load is $P = 100\,\text{N}$ and $E_T = 250\,\text{Pa}$.

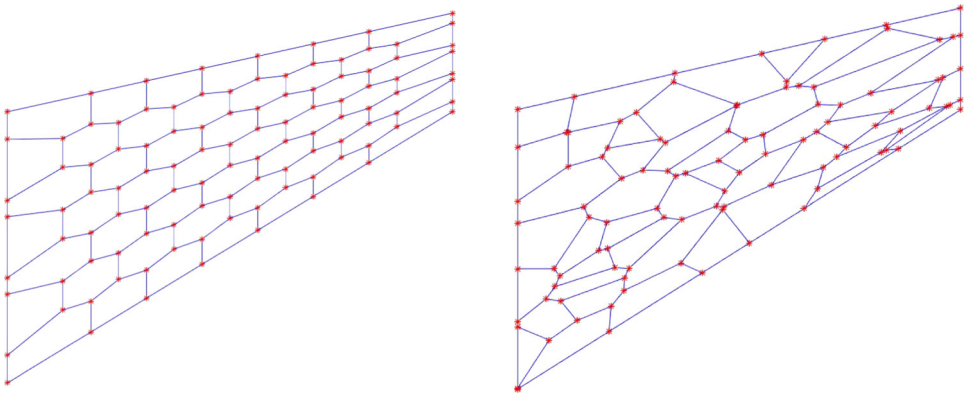

Fig. 2 Cook's membrane problem, showing the hexagonal and Voronoi meshes for $d = 7$

(a) Hex mesh **(b)** Voronoi mesh

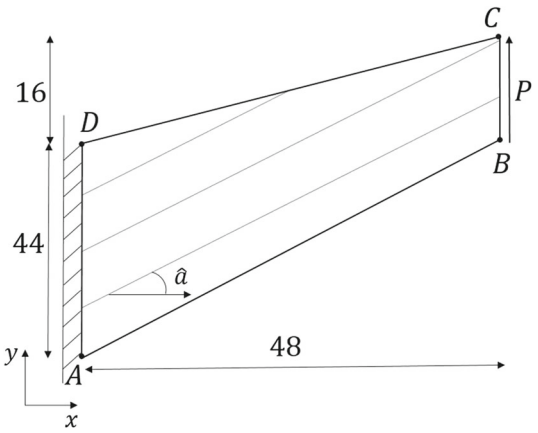

Fig. 3 Cook's membrane problem, showing fibres inclined at $\hat{a} = \frac{\pi}{4}$

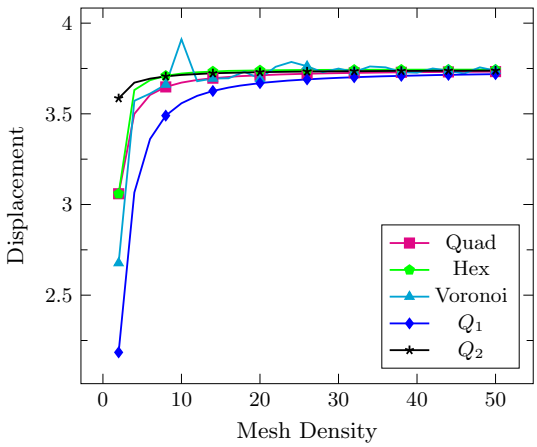

Fig. 4 The Cook problem: convergence test for fibre angle $\hat{a} = \frac{\pi}{4}$ and $p = 5$

This test problem has no analytical solution. The vertical displacement at point C is recorded.

Figure 4 shows a convergence plot of tip displacement versus mesh density for fibre angle $\hat{a} = \frac{\pi}{4}$, as illustrated in Fig. 3, and with $p = 5$, for the VEM formulation with the three candidate meshes, and for standard finite element formulations. The various VEM formulations are seen to exhibit degrees of accuracy comparable to that of the Q_2 approximation, where the Q_2 approximation is assumed to accurately represent the solution.

The results that follow have been generated using meshes with a density of $d = 50$.

Figure 5 shows semilog plots of tip displacement versus p for $1 \leq p \leq 10^5$ and for fibre angles $\hat{a} = \frac{\pi}{4}$ and $\hat{a} = \frac{\pi}{9}$. The well-known locking behaviour of Q_1 is clear in the isotropic limit ($p \to 1$). On the other hand, the VEM formulation using quadrilaterals is not equivalent to the conventional Q_1 formulation, and is locking-free. We note, additionally, the rapid transition to locking behaviour of the Q_1 formulation as $p \to 1$. The formulation exhibits severe locking for $p = 1$, for $p = 1.01$ we observe mild locking behaviour and with $p = 1.02$ the behaviour is near locking-free. Thus the locking behaviour of the Q_1 formulation is not discontinuous at $p = 1$.

Figure 6 shows a plot of tip displacement versus fibre orientation for a nearly inextensible material ($p = 10^5$). Again, we note the poor performance and locking behaviour of Q_1 over most of the range, and on the other hand the robust behaviour of the VEM formulation. The Q_2 element displays sub-optimal accuracy for fibre angles greater than $\hat{a} = \frac{\pi}{2}$ and close to zero. This is somewhat surprising, in that the behaviour of this element in the near-inextensible limit would be expected to mirror its good performance for near-incompressibility. On the other hand, while the element has been shown to be uniformly convergent for incompressible materials, there does not exist a corresponding analysis for near-inextensibility, to the best of the authors' knowledge. Such an analysis could shed light on the behaviour seen in Fig. 6.

The beam problem This problem consists of a beam subjected to a linearly varying load at its right edge, and pinned at its left extrema, as depicted in Fig. 7. The load has maximum and minimum values of $F_{max} = \pm 30\,\text{N}$. The beam

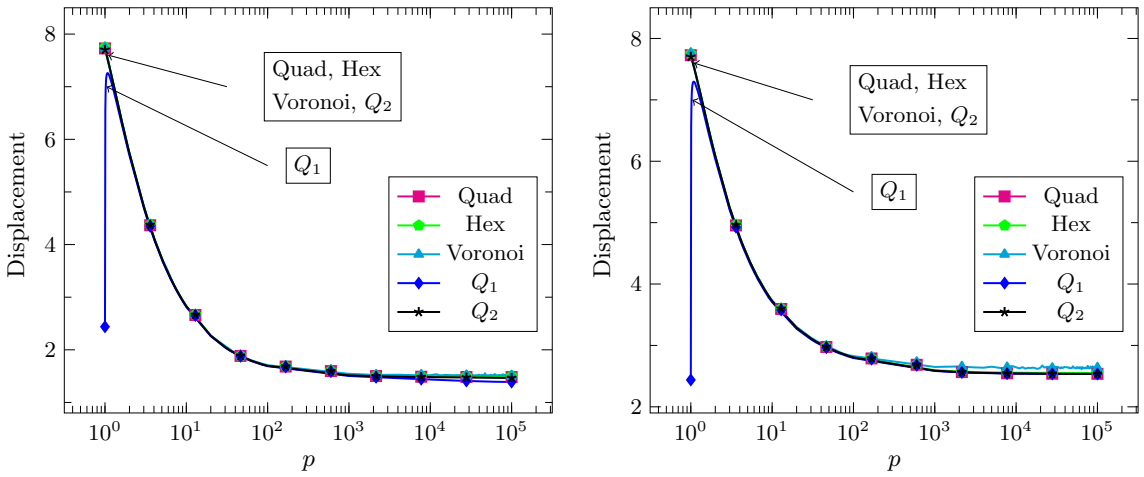

(a) $\hat{a} = \frac{\pi}{4}$ **(b)** $\hat{a} = \frac{\pi}{9}$

Fig. 5 The Cook problem: tip displacement versus p for **a** fibre direction $\hat{a} = \frac{\pi}{4}$; **b** fibre direction $\hat{a} = \frac{\pi}{9}$

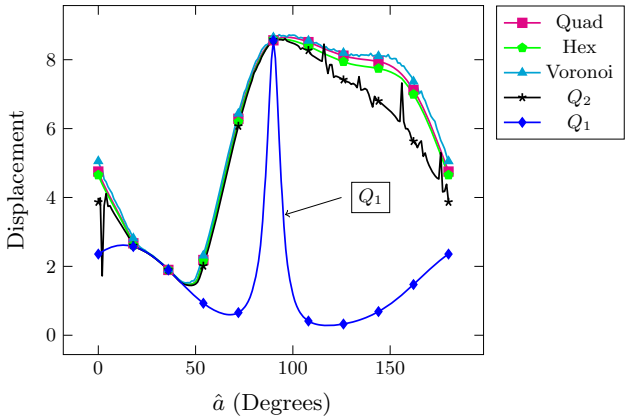

Fig. 6 The Cook problem: tip displacement versus fibre orientation, for $p = 10^5$

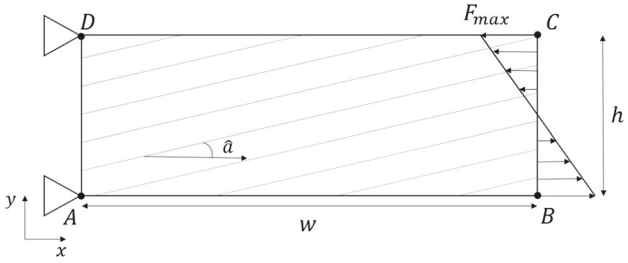

Fig. 7 The beam problem, showing fibres inclined at $\hat{a} = \frac{\pi}{4}$

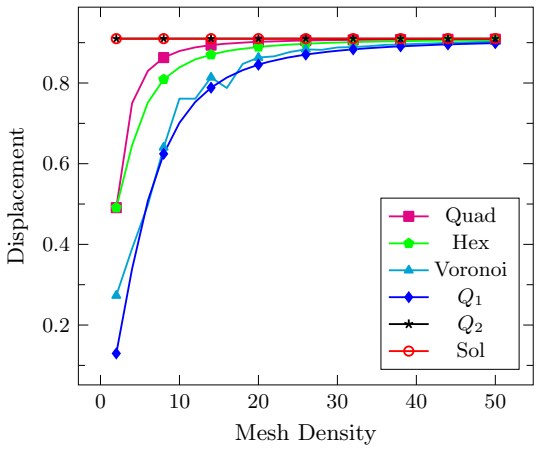

Fig. 8 The beam problem: convergence test for fibre angle $\hat{a} = \frac{\pi}{4}$ and $p = 5$

has width $w = 10$, height $h = 2$ and Young's Modulus of $E_T = 1500\,\text{Pa}$. The vertical displacement at point C is recorded.

The displacement of point C is given by [20]

$$u(x, y) = \frac{2F_{max}}{h}\left[\mathbb{S}_{11}xy + \frac{\mathbb{S}_{31}}{2}\left(y^2 - \frac{h^2}{4}\right)\right], \tag{4.1}$$

$$v(x, y) = \frac{F_{max}}{h}\left[\mathbb{S}_{21}\left(y^2 - \frac{h^2}{4}\right) - \mathbb{S}_{11}x^2\right]; \tag{4.2}$$

the coefficients $\mathbb{S}_{ij}$ are lengthy functions of the material constants, and are given in the Appendix to [20].

Figure 8 shows a convergence plot of tip displacement versus mesh density for a fibre orientation of $\hat{a} = \frac{\pi}{4}$, and with $p = 5$. It is seen that for the various VEM meshes the convergence behaviour is similar to that of the Q_2 mesh for sufficiently fine meshes.

The results that follow have been generated using meshes with a density of $d = 50$.

Figure 9 shows semilog plots of tip displacement versus p for $1 \le p \le 10^5$ for fibre angles of $\hat{a} = \frac{\pi}{4}$ and $\hat{a} = \frac{\pi}{9}$. Again, as with the Cook problem, the VEM solutions are locking-free and display high accuracy. As pointed out in [20], for

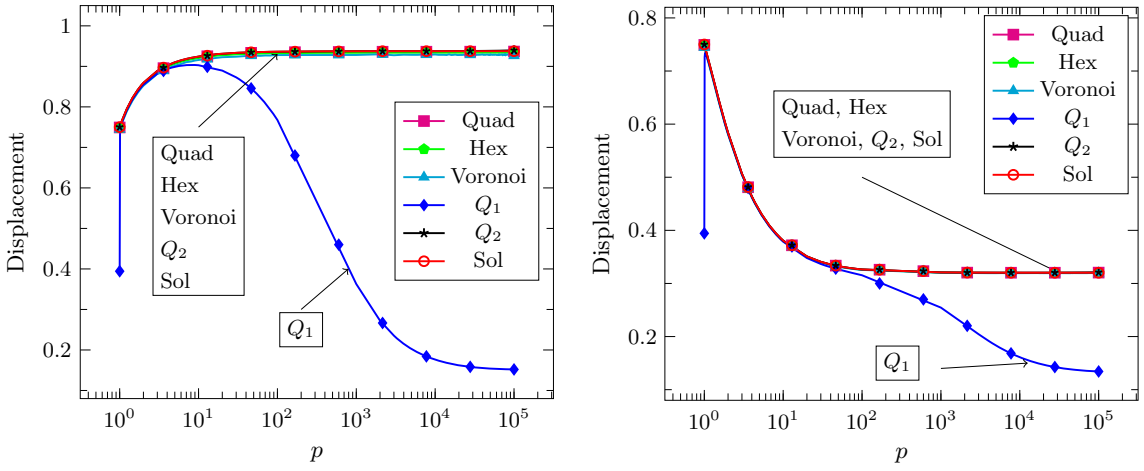

Fig. 9 Beam problem: tip displacement versus p for fibre angle **a** $\hat{a} = \frac{\pi}{4}$; **b** $\hat{a} = \frac{\pi}{9}$

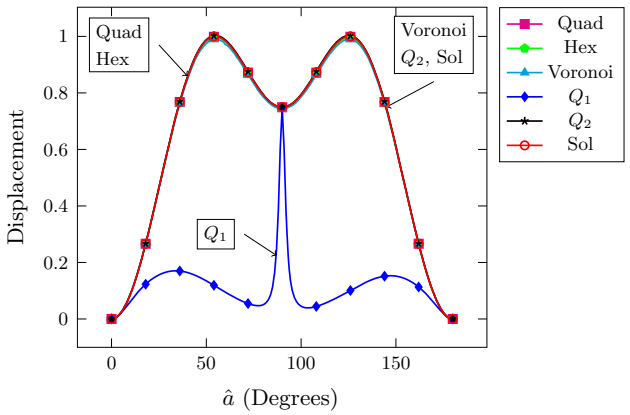

Fig. 10 The beam problem: tip displacement versus fibre orientation, for $p = 10^5$

mild anisotropy, that is, low values of p, the tendency to lock for the Q_1 mesh is mitigated as a result of the Lamé parameter being bounded for $p > 1$ in conditions of near-incompressibility, with ν very close to 0.5. This behaviour is evident in Fig. 9, where the Q_1 mesh is seen to be locking-free for $p > 1$ and for p up to $p \approx 10$ for fibre angle $\hat{a} = \frac{\pi}{4}$, and $p \approx 100$ for fibre angle $\hat{a} = \frac{\pi}{9}$. However, the rapid transition to locking behaviour of the Q_1 formulation as $p \to 1$ is again evident, as observed in Fig. 5.

Figure 10 shows a plot of tip displacement versus fibre orientation for the case of near-inextensibility ($p = 10^5$). Again, we note poor performance of Q_1 and robust and accurate behaviour of the VEM formulations. In contrast to the result for the Cook problem, here the Q_2 element demonstrates equally accurate behaviour.

To investigate the effects of $p < 1$ we present in Fig. 11 the beam problem, as above, with $\hat{a} = \frac{\pi}{4}$. We consider Poisson's ratios of $\nu = 0.3$ and $\nu = -0.5$ in Fig. 11a, b respectively. To satisfy the conditions for pointwise stability we require for a Poisson's ratio of $\nu = 0.3$ that $p > 0.2571$, and for $\nu = -0.5$ that $p > \frac{1}{3}$.

Figure 11a shows a plot of tip displacement versus p for the case $\nu = 0.3$. We note the accuracy of the VEM formulations and the biquadratic approximation throughout the domain as both closely match the analytical solution. The bilinear approximation exhibits accuracy for values of p corresponding to mild anisotropy, i.e for p up to $p \approx 10$. As the degree of anisotropy increases the bilinear approximation exhibits locking behaviour consistent with that seen in Fig. 9.

Figure 11b shows a plot of tip displacement versus p for the case $\nu = -0.5$. We note similar behaviour to that seen in Fig. 11a, with high accuracy displayed by the VEM formulations and the biquadratic approximation throughout the domain, and locking behaviour exhibited by the bilinear approximation as the degree of anisotropy increases. Additionally, we note inaccuracy and locking of the bilinear approximation as $p \to \frac{1}{3}$.

4.2 Non-homogeneous materials: variable fibre orientation

For a given distribution of fibre directions $\boldsymbol{a}(\boldsymbol{x})$ it follows that some approximation has to be made for $\boldsymbol{a}(\boldsymbol{x})$ within each element so as to preserve the general approach to carry out VEM computations. A simple option would be to approximate $\boldsymbol{a}$ by its centroidal value. However, such an approximation can be somewhat inaccurate for situations in which the fibre orientation varies significantly across a length scale comparable to mesh size. A more reliable approach is to use the average fibre direction at the element nodes; this approach is observed to yield more stable and faster convergence. When dealing with rapidly varying fibre directions a more stable

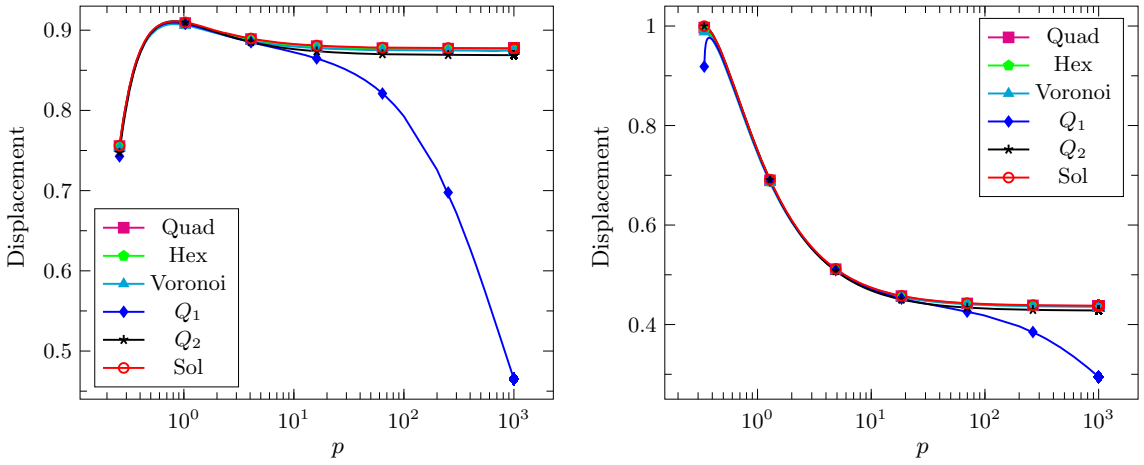

(a) $\nu = 0.3$ **(b)** $\nu = -0.5$

Fig. 11 The beam problem: tip displacement versus p with $\hat{a} = \frac{\pi}{4}$, for **a** $\nu = 0.3$; and **b** $\nu = -0.5$

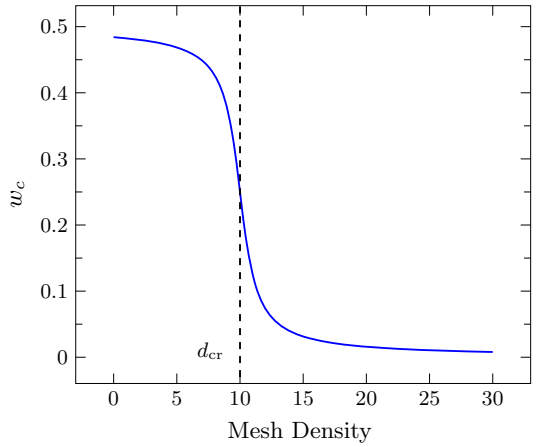

Fig. 12 The weight w_c as a function of mesh density d

approach was achieved by using a weighted average of the fibre direction at the centroid and the average direction at the vertices. This approach applies an equal weighting to the centroidal direction and the average of its nodal values for very coarse meshes; for finer meshes, that is, as the mesh density increases, the weighting of the centroidal value decreases rapidly. Thus for very fine meshes and rapidly varying fibre directions, it is the nodal average that dominates. With the mesh density denoted by d, the centroidal weight w_c is defined by

$$w_c = \frac{\frac{\pi}{2} + \arctan(d_{\text{cr}} - d)}{2\pi} . \tag{4.3}$$

This function is shown in Fig. 12. Here d_{cr} is a user-defined critical mesh density beyond which the value of the weight drops rapidly.

The average fibre direction $\boldsymbol{a}$ is then given by

$$\boldsymbol{a}_{\text{ave}}|_E = w_c \boldsymbol{a}(\boldsymbol{x}_c) + (1 - w_c)\frac{1}{N}\sum_{i=1}^{N} \boldsymbol{a}(\boldsymbol{x}_i) , \tag{4.4}$$

where, as before, N denotes the number of nodes of element E, and $\boldsymbol{x}_c$ and $\boldsymbol{x}_i$ are respectively the coordinates of the element centroid and node i. We then approximate the elasticity tensor on an element E by

$$\mathbb{C}|_E \simeq \mathbb{C}(\boldsymbol{a}_{\text{ave}}) . \tag{4.5}$$

The critical density used is problem specific as it depends on the degree of variation in fibre orientation. However, for simplicity a critical density of $d_{\text{crit}} = 10$ was used as it worked well across a range of problems.

Except where otherwise stated, Poisson's ratio is set at $\nu = 0.3$ in the examples that follow.

We present results for two families of fibre distributions, corresponding to curves $y = c + f(x)$ where $f(x)$ is chosen to be, respectively, $(x-24)^2(x-12)(x-36)$ and $2\sin x$. The polynomial distribution corresponds to mild variation with position, while the sinusoidal distribution is a more severe test of performance under conditions of rapidly varying direction. Figure 13 shows schematically the curves corresponding to these two cases for the Cook problem, one of the examples considered in what follows.

Cook's membrane problem Figure 14a, b show the tip displacement as a function of mesh density for fibres corresponding to the quartic distribution, with $p = 5$, and in which the value of $\boldsymbol{a}$ is based respectively on its value at the element centroids and the average of its values at the nodes. We note smooth and stable convergence of the VEM, with the

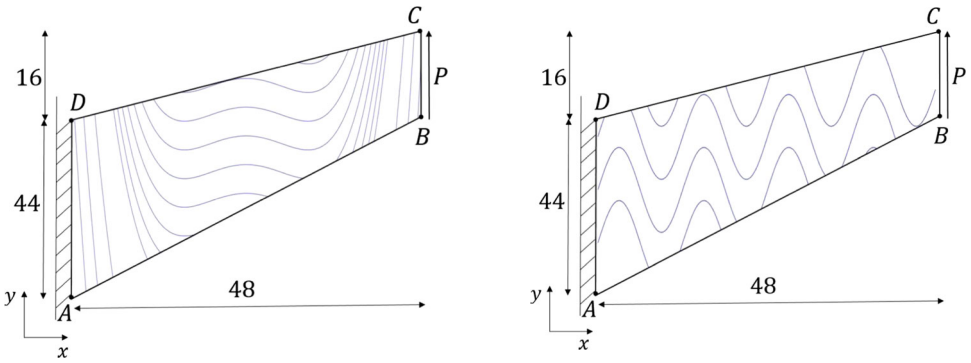

(a) Quartic distribution **(b)** Sinusoidal distribution

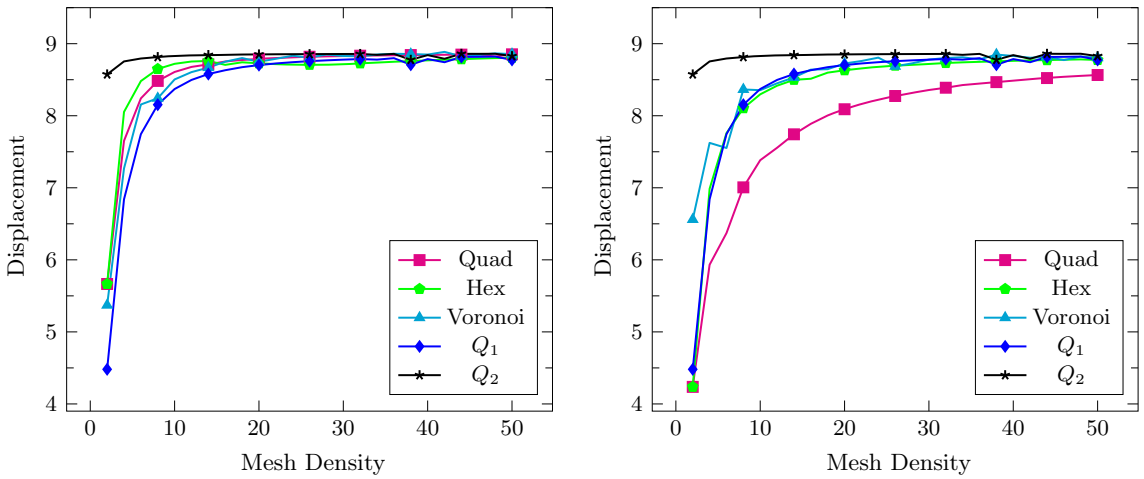

(a) Centroidal value **(b)** Average nodal value

Fig. 13 Cook's membrane problem with curves showing variable fibre orientation for **a** quartic, and **b** sinusoidal distributions

Fig. 14 Tip displacement versus mesh density for Cook's membrane problem for $p = 5$, with fibre directions defined by quartic curves, and using **a** the centroidal value of $\boldsymbol{a}$; **b** the average of nodal values of $\boldsymbol{a}$

quadrilateral VEM mesh performing somewhat more poorly for the case in which the average nodal value of $\boldsymbol{a}$ is used.

Figure 15 shows tip displacement as a function of mesh density for fibres corresponding to the sinusoidal distribution. In Fig. 15a we calculate $\boldsymbol{a}_{\text{ave}}$ based on its value at the element centroid. Again we see good performance by the VEM elements, with an accuracy comparable to that of Q_2. In contrast to the results for polynomial variation in Fig. 14a, b, the coarse-mesh behaviour is somewhat erratic, with a smooth dependence on mesh density only after $d \approx 25$. Figure 15c, d present results for the cases in which, respectively, firstly an equal weighting of centroidal and nodal values of $\boldsymbol{a}$ is used, and secondly, using (4.4), a varying weight is used. Similar behaviour is seen when compared with the results in Fig. 14b, though the dependence on mesh density becomes smoother for coarser meshes at $d \approx 15$.

Next, we consider behaviour in the near-incompressible limit, with $\nu = 0.49995$. Figure 16a, b show tip displacement as a function of p, for the quartic and sinusoidal fibre distributions respectively. For the polynomial fibre distribution the centroidal values of fibre direction are used, while the weighted method is used for the sinusoidal distribution. There is little variation in the performance of the various VEM meshes, though for the Voronoi mesh and for near-inextensibility small scatter is observed. The sub-optimal behaviour of the Q_2 mesh seen in the Cook example in Fig. 6 is not evident here. The Q_1 mesh again displays locking behaviour except in a narrow range of mild anisotropy.

Beam in bending We consider next the problem of a beam in bending, shown in Fig. 17, with boundary conditions slightly different to those shown in Fig. 7; the left edge is now constrained horizontally and pinned at the bottom left corner. The fibre distributions considered are once again quartic and sinusoidal, as for the Cook problem, and are depicted in Fig. 17. However, the quartic distribution is now defined by $y = (x-5)^2\,(x-2.5)\,(x-7.5) + c$, and the sinusoidal distribution is as defined previously. The vertical displacement at point C is recorded. A value of Poisson's ratio of $\nu = 0.3$ is used, except where indicted otherwise.

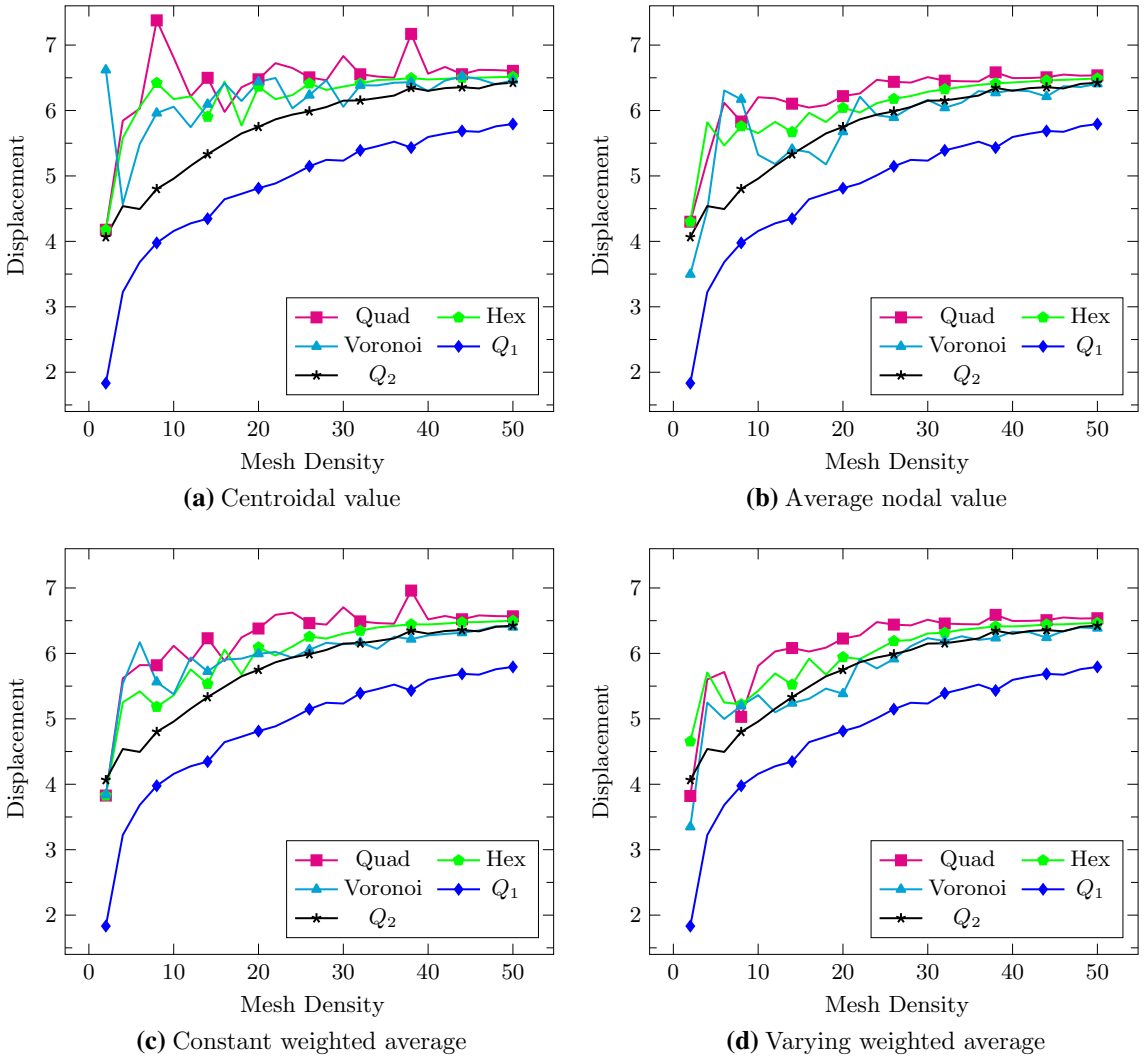

(a) Centroidal value **(b)** Average nodal value

(c) Constant weighted average **(d)** Varying weighted average

Fig. 15 Tip displacement versus mesh density for Cook's membrane problem and with fibre directions defined by curves $2\sin x$, and using **a** the centroidal value of $\boldsymbol{a}$; **b** the average of nodal values of $\boldsymbol{a}$; **c** equal weighting of nodal and centroidal values; and **d** a varying weighted average as in (4.3) and (4.4)

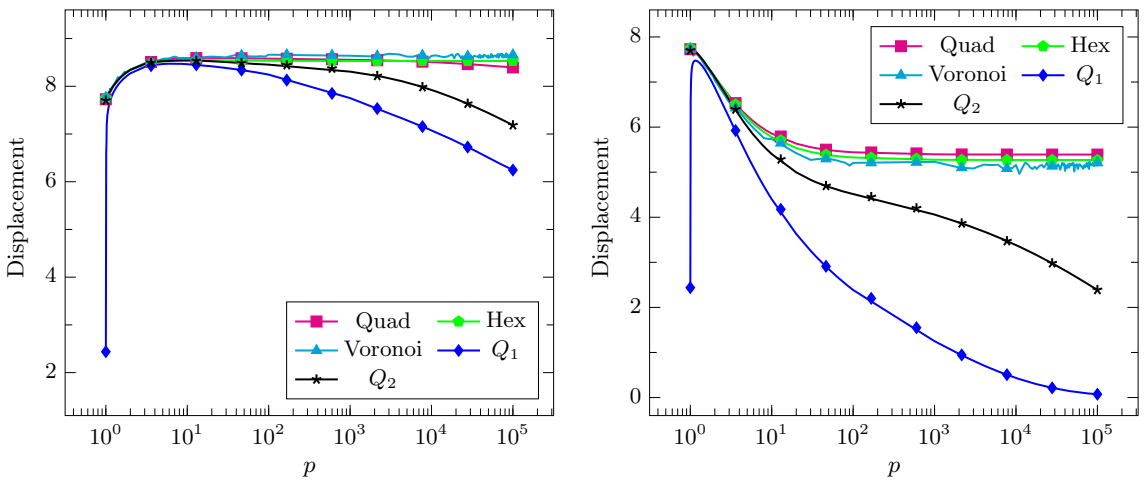

(a) Quartic distribution **(b)** Sinusoidal distribution

Fig. 16 Tip displacement versus p for the Cook problem, for near-incompressibility and using **a** the quartic, and **b** the sinusoidal fibre distributions

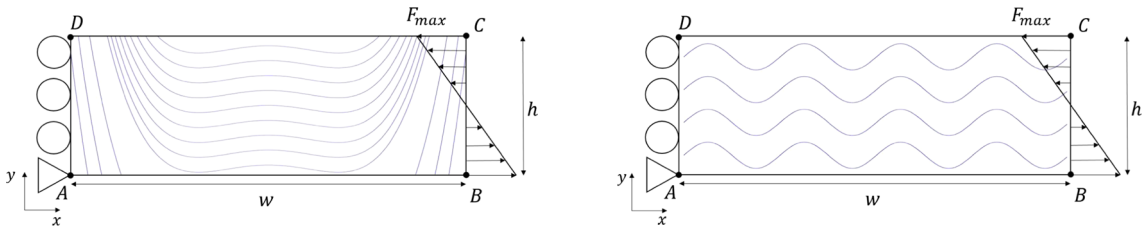

(a) Quartic distribution **(b)** Sinusoidal distribution

Fig. 17 Quartic and sinusoidal fibre distributions for the beam in bending problem

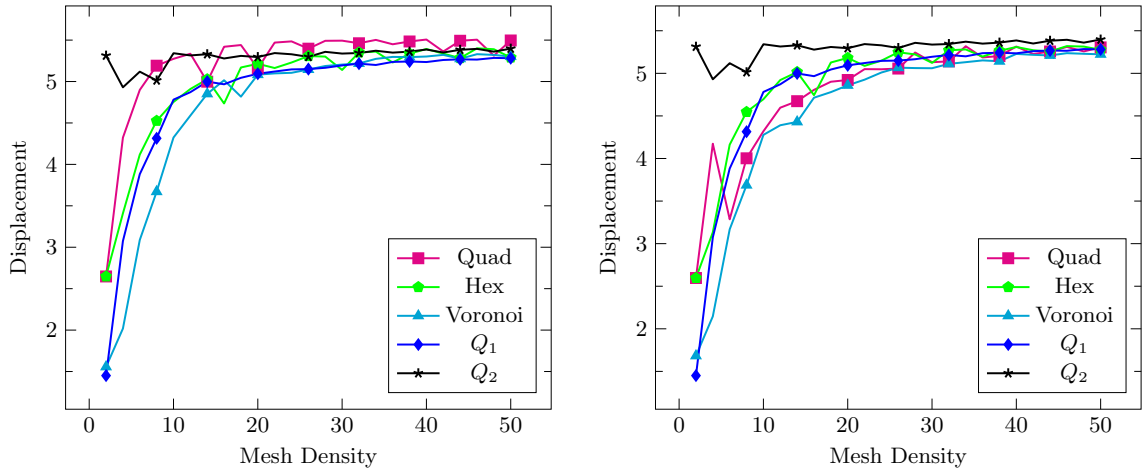

(a) Centroidal value **(b)** Average nodal value

Fig. 18 Tip displacement versus mesh density for the beam in bending problem, with $p = 5$, and fibre directions defined by a quartic polynomial, using **a** the centroidal value of $\boldsymbol{a}$; **b** the average of nodal values of $\boldsymbol{a}$

In Fig. 18a, b we present convergence plots of vertical displacement versus mesh density, for mild anisotropy; that is, $p = 5$, for the quartic distribution of fibres, and with $\boldsymbol{a}_{\text{ave}}$ calculated using respectively the centroidal value, and the average nodal value. We note stable convergence in all cases. For the case in which the average nodal direction is used, it is seen that the standard Q_2 element performs best for coarse meshes.

Figure 19 shows tip displacement as a function of mesh density for a sinusoidal distribution of fibres. In Fig. 19a we calculate $\boldsymbol{a}_{\text{ave}}$ based on its centroidal value. Again we see good performance by the VEM elements, though the Q_2 mesh performs best. Rapid numerical convergence is however observed after a density of $d \approx 25$.

As with the Cook problem, we next consider behaviour in the near-incompressible limit with $\nu = 0.49995$. Figure 20 shows tip displacement as a function of p, for the quartic and sinusoidal fibre distributions. For the polynomial fibre distribution the average value of fibre direction at the vertices is used, while the weighted method is used for the sinusoidal distribution. There is little variation in the performance of the various VEM meshes, though for the Voronoi mesh and for near-inextensibility small scatter is again observed. The Q_2 mesh performs rather poorly, displaying some evidence of mild locking. This should be compared with the sub-optimal behaviour seen in Fig. 6 for constant fibre directions. Except in a narrow range of mild anisotropy, the Q_1 mesh displays locking behaviour.

4.3 Error analysis

To further investigate the performance of the VEM we present here a convergence analysis. We consider the beam problem depicted in Fig. 7 and set $p = 5$ and $\nu = 0.49995$. In this section we present error estimates of both the displacement and stress fields using an L^2 norm.

Displacement error The L^2 norm of displacement is defined by

$$\mathrm{E}_{u_i,\Omega} = \left(\sum_{i=1}^{N} \int_E \left| u_i - u_i^h \right|^2 d\Omega \right)^{0.5} = ||u_i - u_i^h||_0. \quad (4.6)$$

This definition poses problems for VEMs as it requires the computation of $\boldsymbol{u}_h$ over the area of an element. As the basis

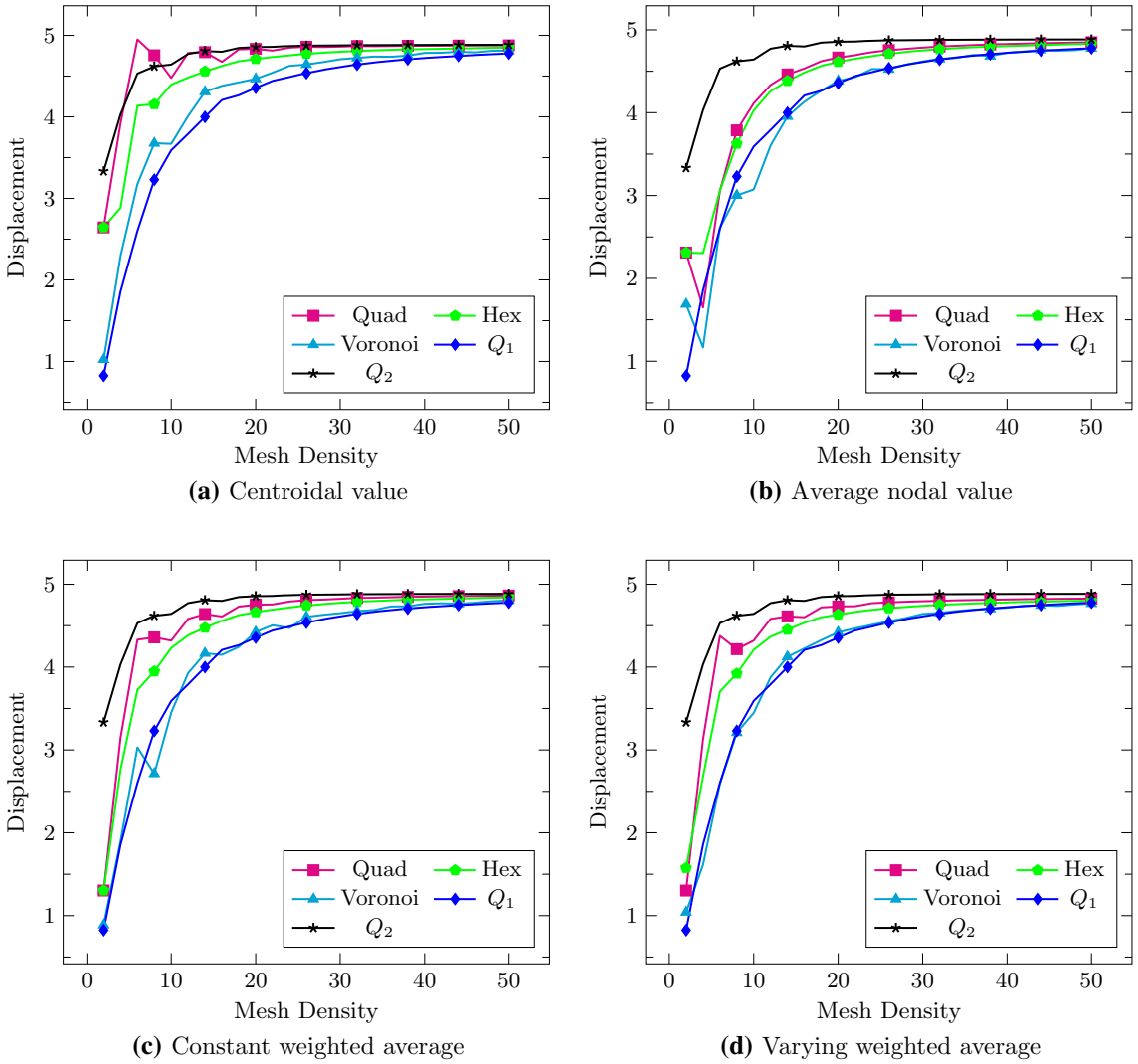

Fig. 19 Tip displacement versus mesh density for the beam in bending problem, with fibre directions defined by curves $2\sin x$, and using **a** the centroidal value of $\boldsymbol{a}$; **b** the average of nodal values of $\boldsymbol{a}$; **c** equal weighting of nodal and centroidal values; and **d** a varying weighted average as in (4.3) and (4.4)

functions $\boldsymbol{\varphi}$ are defined implicitly, and thus only known on the element boundary, some approximation of the displacement within an element is required. A simple approach would be to decompose a polygonal element into a collection of triangular sub-elements and to use the standard P_1 (linear) triangular shape functions as interpolants. Such a decomposition is undesirable and not in keeping with the spirit of the VEM. We therefore present an alternative approach in which the displacement is approximated by a linear polynomial, at an element level, such that its nodal values are closest to the degrees of freedom $\boldsymbol{d}$ in the sense of least squares. We minimise

$$F(\boldsymbol{d}_1) = \frac{1}{2}\left|\boldsymbol{d} - \boldsymbol{d}_1\right|^2 \tag{4.7}$$

$$= \frac{1}{2}\left(\boldsymbol{d}^T\boldsymbol{d} - 2\boldsymbol{s}^T\boldsymbol{D}^T\boldsymbol{d} + \boldsymbol{s}^T\boldsymbol{D}^T\boldsymbol{D}\boldsymbol{s}\right) \tag{4.8}$$

with respect to the independent degrees of freedom $\boldsymbol{s}$. The minimiser satisfies

$$(\boldsymbol{D}^T\boldsymbol{D})\boldsymbol{s} = \boldsymbol{D}^T\boldsymbol{d}, \tag{4.9}$$

and the degrees of freedom of the linear polynomial are then given by

$$\boldsymbol{s} = (\boldsymbol{D}^T\boldsymbol{D})^{-1}\boldsymbol{D}^T\boldsymbol{d}. \tag{4.10}$$

We can then express (4.6) as

$$\mathrm{E}_{u_i,\Omega} = \left(\sum_{i=1}^{N}\int_E \left|u_i - m_{ij}s_j\right|^2 d\Omega\right)^{0.5}, \tag{4.11}$$

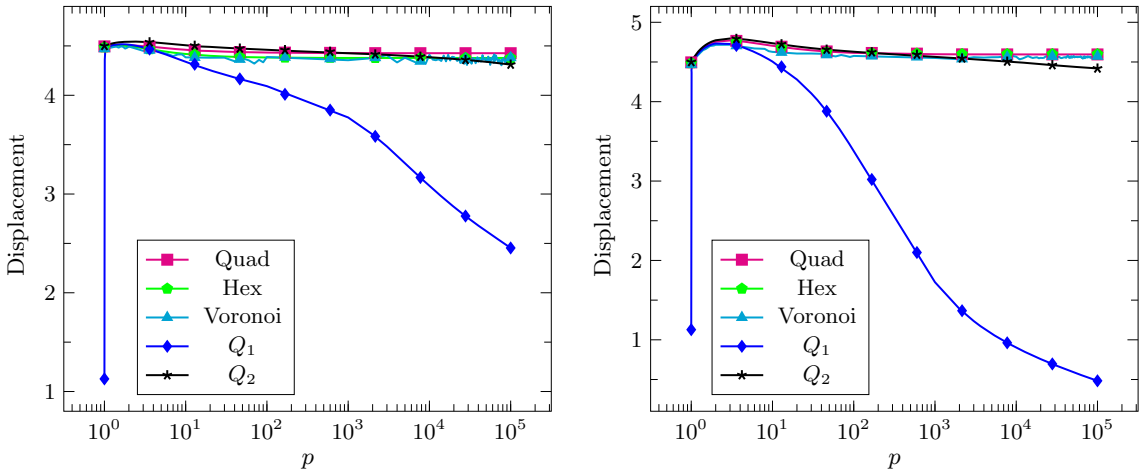

(a) Quartic distribution **(b)** Sinusoidal distribution

Fig. 20 Tip displacement versus p for the beam in bending problem, for near-incompressibility and using **a** the quartic, and **b** the sinusoidal fibre distributions

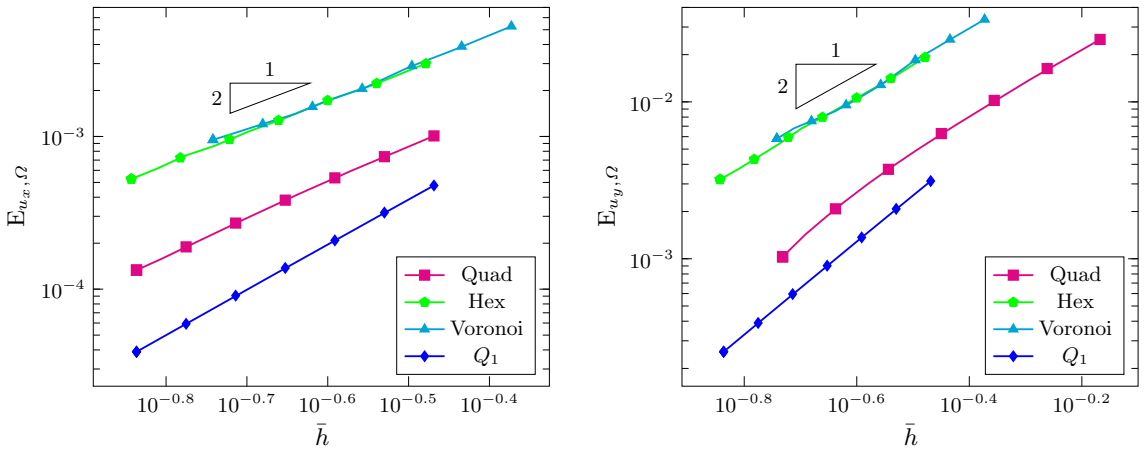

(a) x-displacement **(b)** y-displacement

Fig. 21 The beam problem: L^2 error versus mean element diameter $\bar{h}$ for **a** x-displacement; and **b** y-displacement

where $\boldsymbol{m}$ is the matrix of linear basis monomials given by

$$\boldsymbol{m} = \begin{bmatrix} 1 & 0 & \xi & 0 & \eta & 0 \\ 0 & 1 & 0 & \xi & 0 & \eta \end{bmatrix}. \tag{4.12}$$

Figure 21a, b show plots of L^2 error, as defined by (4.11), versus mean element diameter $\bar{h}$ for displacements in the $x-$ and $y-$directions respectively. We note, in both figures, that the convergence rate, as indicated by the gradient, is approximately equal to 2 for all formulations as is expected. Further, we note that the Q_1 formulation has a very slightly steeper gradient than that of the VEM formulations. This is likely due to the bilinear interpolation of the degrees of freedom used for the Q_1 formulation in calculating the error, as opposed to the linear polynomial approximation used for the VEM formulations, and does not necessarily imply greater accuracy of the respective degrees of freedom.

To further assess the performance of the VEM, and to investigate the small differences in convergence rate between the VEM formulations and the bilinear approximation, we propose an error measure considering only behaviour along element boundaries. Such an error estimate would require no approximations of the displacements beyond those made during the original formulation of the method. Further, it would allow for a more accurate comparison of the accuracy of the degrees of freedom of the VEM formulations relative to those of the bilinear approximation. We define this edge-based error norm as

$$\mathrm{E}_{u_i,\Gamma} = \left(\sum_{i=1}^{n_e} \int_e \left| \frac{u_i - u_i^h}{L} \right|^2 d\Gamma \right)^{0.5}, \tag{4.13}$$

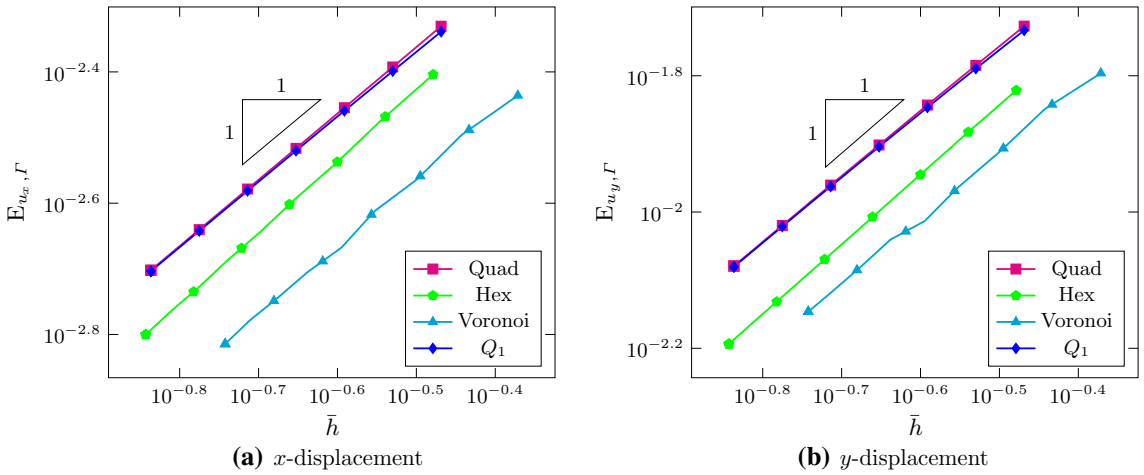

(a) x-displacement **(b)** y-displacement

Fig. 22 The beam problem: L^2 edge error versus mean element diameter $\bar{h}$ for **a** x-displacement; and **b** y-displacement

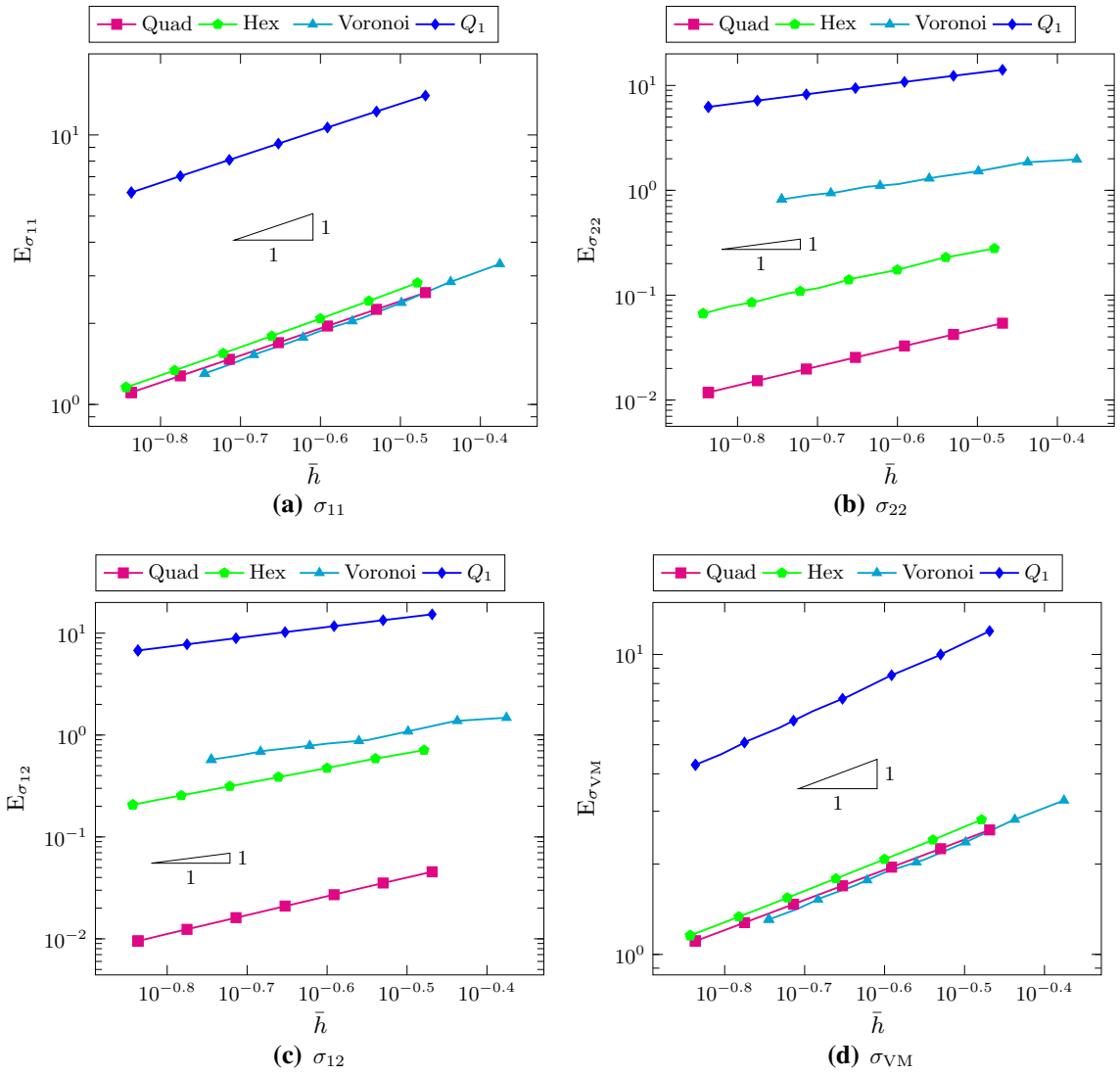

(a) σ_{11} **(b)** σ_{22} **(c)** σ_{12} **(d)** σ_{VM}

Fig. 23 The beam problem: L^2 stress error versus mean element diameter $\bar{h}$ for **a** σ_{11}; **b** σ_{22}; **c** σ_{12} and; **d** σ_{VM}

where L denotes the length of all unique edges in a mesh, and n_e is the number of unique edges.

Figure 22a, b show plots of L^2 edge error, as defined by (4.13), versus mean element diameter $\bar{h}$ for displacements in the x- and y-directions respectively. We note, in both figures, that the convergence rate is approximately equal to 1 for all formulations. Further, the convergence behaviour of the VEM Quad formulation closely matches that of the bilinear approximation. Thus the accuracy of the degrees of freedom of the two formulations are comparable, and the slight discrepancy in the gradients noted in Fig. 21 is therefore a result of the different interpolants used in computing the error and not due to differences in accuracy of the degrees of freedom.

Stress error We make use of an L^2 norm as an error estimate of the stress field with the error defined as

$$\mathrm{E}_{\sigma_{ij}} = \left(\sum_{i=1}^{N} \int_E \left| \sigma_{ij} - \sigma_{ij}^h \right|^2 d\Omega \right)^{0.5}. \tag{4.14}$$

To determine the stress field associated with an element we employ the projection operator, allowing (4.14) to be expressed as

$$\mathrm{E}_{\sigma_{ij}} = \left(\sum_{i=1}^{N} \int_E \left| \sigma_{ij} - (\mathbb{C}\Pi \boldsymbol{u}_h)_{ij} \right|^2 d\Omega \right)^{0.5}. \tag{4.15}$$

As an additional stress measure we introduce the equivalent Von Mises stress σ_{VM} given by

$$\sigma_{\mathrm{VM}} = \sqrt{\sigma_{11}^2 - \sigma_{11}\sigma_{22} + \sigma_{22}^2 + 3\sigma_{12}}. \tag{4.16}$$

Figure 23 shows plots of the L^2 error of the stress fields, as defined by (4.15), versus mean element diameter $\bar{h}$. Figure 23a, b, c and d plot the error for σ_{11}, σ_{22}, σ_{12} and the equivalent Von Mises stress σ_{VM} respectively. We note in all cases a convergence rate, as indicated by the gradient, of approximately 1 as expected. Furthermore, the convergence rate of the stresses associated with the VEM formulations are comparable to those of the bilinear approximation in which the stress field is not assumed to be constant.

The convergence rates we have presented conform with those presented in [21] and [22] using a mixed formulation and stress recovery procedure on degenerate patches respectively. Both works considered the case of isotropic elasticity, however, it is noteworthy that similar convergence results were obtained without adaptation or extension of the method.

5 Concluding remarks

In this work we have formulated and implemented a virtual element method for plane transversely isotropic elasticity, making provision for homogeneous as well as non-homogeneous bodies. In the latter case, various options for taking account of the non-constant elasticity tensor are investigated. The formulations have been studied numerically through two model problems, and for three different kinds of polygonal meshes. The results have been compared against those obtained using conventional conforming finite element approximations with bilinear and biquadratic approximations.

The VEM approximations are found to be locking-free for both near-incompressibility and near-inextensibility, without the need to make modifications to the formulation. In the case of finite element approximations, the well-known volumetric locking behaviour of bilinear approximations is evident, except for a range of parameters corresponding to mild anisotropy. This behaviour is consistent with what has been shown in [20]; for mild anisotropy the Lamé parameter related to the volumetric response is bounded. Locking does however occur in the inextensible limit. Further, the VEM formulations are shown to exhibit the expected convergence rates for both displacement and stress fields, again, requiring no modification to the method.

There have been few studies of transverse isotropy in the context of development of new finite element and related methods. The present study and the work cited above constitute two new contributions. Further work is in progress on alternative formulations such as, for example, the use of discontinuous Galerkin methods. The extension to problems involving nonlinear material behaviour and large deformations is also in progress. It would be of interest to investigate the extension of the work presented here to include higher order VEMs as well as problems in three dimensions.

Acknowledgements This work was carried out with support from the National Research Foundation of South Africa, through the South African Research Chair in Computational Mechanics. The authors acknowledge with thanks this support.

References

1. Belytschko T, Liu WK, Moran B, Elkhodary K (2014) Nonlinear finite elements for continua and structures. Wiley, Hoboken
2. Wriggers P (2008) Nonlinear finite element methods. Springer, Berlin
3. Boffi D, Brezzi F, Fortin M (2013) Mixed finite element methods and applications. Springer, New York. https://doi.org/10.1007/978-3-642-36519-5
4. Hughes T (1987) The finite element method. Linear static and dynamic finite element analysis. Prentice-Hall, Englewood Cliffs
5. Arnold D, Brezzi F, Cockburn B, Marini L (2002) Unified analysis of discontinuous Galerkin methods for elliptic prob-

lems. SIAM J Numer Anal 39:1749–1779. https://doi.org/10.1137/S0036142901384162
6. Grieshaber B, McBride A, Reddy B (2015) Uniformly convergent interior penalty methods using multilinear approximations for problems in elasticity. SIAM J Numer Anal 53:2255–2278. https://doi.org/10.1137/140966253
7. Hansbo P, Larson M (2002) Discontinuous Galerkin methods for incompressible and nearly incompressible elasticity by Nitsche's method. Comput Methods Appl Mech Eng 191:1895–1908. https://doi.org/10.1016/S0045-7825(01)00358-9
8. Wihler TP (2004) Locking-free DGFEM for elasticity problems in polygons. IMANJA 24(1):45–75. https://doi.org/10.1093/imanum/24.1.45
9. Beirão da Veiga L, Brezzi F, Cangiani A, Manzini G, Marini L, Russo A (2013) Basic principles of virtual element methods. Math Models Methods Appl Sci 23(01):199–214. https://doi.org/10.1142/S0218202512500492
10. Beirão da Veiga L, Brezzi F, Marini L, Russo A (2014) The hitchhiker's guide to the virtual element method. Math Models Methods Appl Sci 24:1541–1573. https://doi.org/10.1142/S021820251440003X
11. Gain A, Talischi C, Paulino G (2014) On the virtual element method for three-dimensional linear elasticity problems on arbitrary polyhedral meshes. Comput Methods Appl Mech Eng 282:132–160. https://doi.org/10.1016/j.cma.2014.05.005
12. Chi H, Beirão da Veiga L, Paulino G (2017) Some basic formulations of the virtual element method (VEM) for finite deformations. Comput Methods Appl Mech Eng 318:148–192. https://doi.org/10.1016/j.cma.2016.12.020
13. Wriggers P, Reddy B, Rust W, Hudobivnik B (2017) Efficient virtual element formulations for compressible and incompressible finite deformations. Comput Mech 60:253–268. https://doi.org/10.1007/s00466-017-1405-4
14. Artioli E, Beirão da Veiga L, Lovadina C, Sacco E (2017) Arbitrary order 2D virtual elements for polygonal meshes: part II, inelastic problem. Comput Mech 60:643–657. https://doi.org/10.1007/s00466-017-1429-9
15. Beirão da Veiga L, Lovadina C, Mora D (2015) A virtual element method for elastic and inelastic problems on polytope meshes. Comput Methods Appl Mech Eng 295:327–346. https://doi.org/10.1016/j.cma.2015.07.013
16. Wriggers P, Hudobivnik B (2017) A low order virtual element formulation for finite elasto-plastic deformations. Comput Methods Appl Mech Eng 327:459–477. https://doi.org/10.1016/j.cma.2017.08.053
17. Wriggers P, Rust W, Reddy B (2016) A virtual element method for contact. Comput Mech 58:1039–1050. https://doi.org/10.1007/s00466-016-1331-x
18. Wriggers P, Hudobivnik B, Korelc J (2018) Efficient low order virtual elements for anisotropic materials at finite strains. In: Advances in computational plasticity, computational methods in applied sciences. Springer, Berlin. https://doi.org/10.1007/978-3-319-60885-3_20
19. Auricchio F, Scalet G, Wriggers P (2017) Fiber-reinforced materials: finite elements for the treatment of the inextensibility constraint. Comput Mech 60:905–922. https://doi.org/10.1007/s00466-017-1437-9
20. Rasolofoson F, Grieshaber B, Reddy BD (2019) Finite element approximations for near-incompressible and near-inextensible transversely isotropic bodies. Int J Numer Methods Eng 117(6):693–712. https://doi.org/10.1002/nme.5972
21. Artioli E, de Miranda S, Lovadina C, Patruno L (2017) A stress/displacement virtual element method for plane elasticity problems. Comput Methods Appl Mech Eng 325:155–174. https://doi.org/10.1016/j.cma.2017.06.036
22. Artioli E, de Miranda S, Lovadina C, Patruno L (2018) An equilibrium-based stress recovery procedure for the VEM. Int J Numer Methods Eng 117(8):885–900. https://doi.org/10.1002/nme.5983
23. Exadaktylos G (2001) On the constraints and relations of elastic constants of transversely isotropic geomaterials. Int J Rock Mech Min Sci 38:941–956. https://doi.org/10.1016/S1365-1609(01)00063-6
24. Lai WM, Krempl E, Rubin DH (2009) Introduction to continuum mechanics. Elsevier Science & Technology, Amsterdam
25. Artioli E, Beirão da Veiga L, Lovadina C, Sacco E (2017) Arbitrary order 2D virtual elements for polygonal meshes: part I, elastic problem. Comput Mech 60:355–377. https://doi.org/10.1007/s00466-017-1404-5